Preprints of the 19th World Congress
The International Federation of Automatic Control
Cape Town, South Africa. August 24-29, 2014

Vision Based Iterative Learning Control for a Roll to Roll Micro/nano-manufacturing System

Erick Sutanto*. Andrew G. Alleyne*

**Department of Mechanical Science and Engineering, University of Illinois at Urbana Champaign, Urbana, IL, 61081, USA (Tel: (217) 244-9993; e-mail: alleyne@illinois.edu)*

Abstract: Fabrication of nano/micro-scale functional devices oftentimes involves multiple steps. In the context of a continuous or semi-continuous manufacturing process, each fabrication step is performed successively in multiple localized zones. As the substrate or the web traverses downstream in the process flow, proper registration of the pre-existing features is necessary prior to entering the next fabrication zone in order to accurately complement previous manufacturing steps. By performing a direct observation of the pre-existing feature using machine vision, the uncertainty of the feature location can be circumvented. In this paper, a two-layer feedback architecture with a vision sensor in the outer loops is used to visually servo the pre-existing feature on the web. Additionally, the feedback controller is augmented with Norm Optimal Iterative Learning Control (NOILC) to improve the position tracking and tension regulation of the web. Simulation and experimental results show the advantages of implementing NOILC in the R2R system.

Keywords: Iterative Learning Control, Vision, Manufacturing System, 2 DOF Control, Optimal Control

1. INTRODUCTION

Manufacturing systems, which by definition perform the same tasks repeatedly, have benefitted significantly by the incorporation of Iterative Learning Control (ILC) (Arimoto, S; Kawamura, S; Miyazaki 1984)(Arimoto, S; Kawamura, S; Miyazaki 1984). ILC is a method by which specific signals are learned through repeated iterations. This data-driven control technique examines the error from previous iterations to update feedforward input signals in the current trial, resulting in better tracking precision. In recent years, significant works have been performed on the theory (Amann et al. 1996; Gunnarsson & Norrlöf 2001) as well as the practice (Groot Wassink et al. 2006; Barton & Alleyne 2010; Butterworth et al. 2011) of ILC. The interested reader is referred to (Bristow et al. 2006) for a detailed background on the various approaches available. In this article, the authors implement a dual-layer feedback control architecture to accommodate the use of low bandwidth vision based sensors on the Roll to Roll (R2R) system presented in (Sutanto & Alleyne 2013). A lifted NOILC (Lee et al. 2000; Barton & Alleyne 2008) formulation is used to design the ILC input signals which complement the feedback signals.

A R2R system consists of actuated and idler rollers interconnected by a web. A web is described as any flexible material processed in a continuous manner; for example: paper, plastics, textiles and metal strips. The longer term motivation of this work is to transition the Electrohydrodynamic-Jet (E-Jet) printing system (Park & Rogers 2012; Sutanto et al. 2012) from a batch process to a semi-continuous manufacturing process through the R2R system. In the context of a continuous or semi-continuous manufacturing process, fabrication of micro/nano-scale functional devices is often performed successively in multiple localized zones. As the substrate or the web traverses downstream in the process flow, proper registration of the pre-existing features is necessary prior to entering the next fabrication zone in order to accurately complement previous manufacturing steps. Non-collocated sensors, loss of traction between the web and the roller, structural rigidity, and web deformation are several of many factors that contribute to inaccurate feature registration. A direct visual observation helps to circumvent the uncertainty of the feature location on the web.

In the proposed approach, a camera is mounted on an infinitely stiff inertial reference frame and directed normal to the surface of the web observing the features. It is assumed that both the image acquisition and the image processing algorithm take 5 milliseconds to complete. In the dual state feedback architecture discussed in this article, the machine vision provides visual measurement data to the outer loop, which correspond to the instantaneous position of the web. The feedback signals in the outer loop provide reference signals to the inner loop, which is essentially the R2R system previously reported in (Sutanto & Alleyne 2013). All numerical parameters which describe the system dynamics and feedback controller of the R2R system can be found there. In this paper, the authors demonstrate the advantage of complementing the dual-layer feedback architecture with NOILC to improve the tracking precision of the overall system. Additionally, the performance comparison between the coupled and decoupled NOILC formulation is discussed for the system under study.

2. SYSTEM DESCRIPTION

Considered in this article is the R2R system presented in Fig. 1, where two winder rollers and multiple idler rollers are interconnected by a web. The plant model and the feedback control architecture used in this system are developed using the framework described in (Sutanto & Alleyne 2013). Here, $G(s)$ is the frequency domain representation of the closed loop MIMO system. It maps the reference signals $\vec{r} = [r_1 \quad r_2]^T$ to the system outputs $\vec{y} = [y_1 \quad y_2]^T$ as defined in (1), where the subscript 1 and 2 are associated with the web position and tension respectively. The web position, y_1, is measured by a high resolution ring encoder and a load cell measures the tension of the web, y_2. The interested reader can find the numerical values of the system parameters in in (Sutanto & Alleyne 2013).

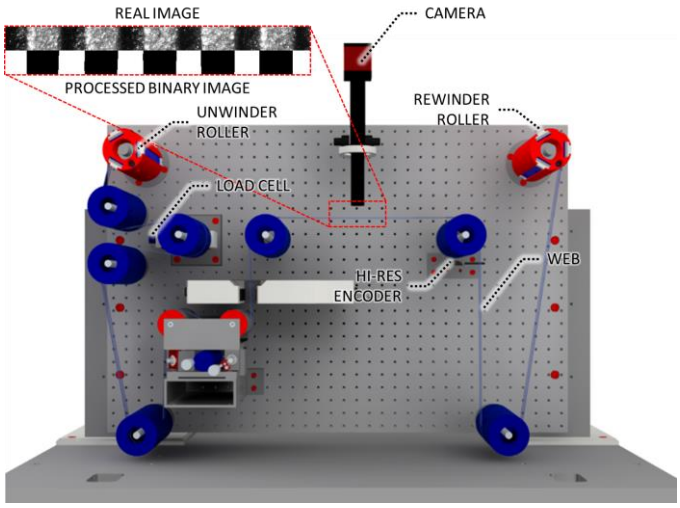

Fig. 1. Configuration of the R2R system Feedback control inner loop can be found in (Sutanto & Alleyne 2013).

$$\begin{bmatrix} Y_1(s) \\ Y_2(s) \end{bmatrix} = \begin{bmatrix} G_{11}(s) & G_{12}(s) \\ G_{21}(s) & G_{22}(s) \end{bmatrix} \begin{bmatrix} R_1(s) \\ R_2(s) \end{bmatrix} \tag{1}$$

As the web traverses downstream in the process flow, the motion of the web as measured by the encoder might not reflect the motion of the pre-existing features on the web. This may be caused by the web stretching and slippage from the rollers. Proper registration of the pre-existing features is necessary to complement previous manufacturing steps. By performing a direct observation of the pre-existing feature using machine vision, the uncertainty of the feature location can be circumvented. As presented in Fig. 1, a camera is directed normal to the surface of the web and is assumed to be mounted on an infinitely stiff inertial reference frame. The top half of the inset in Fig. 1 shows the actual image of the pre-existing features on the web as observed by the camera, while the lower half of the inset shows the processed binary image.

Most high precision electromechanical systems, including $G(s)$, operate at 1 kHz or faster. However, the information extracted from a vision sensor may require a longer time to process and thereby cannot be used as a direct feedback signal for $G(s)$. As presented in the block diagram in Fig. 2, the machine vision is introduced to the R2R system as the position sensor for the outer loop of $G(s)$. Based on the experimental setup, the image acquisition along with the image processing requires at least 5 milliseconds to consistently provide position measurement to the outer loop. In contrast, $G(s)$ samples data every 0.2 millisecond.

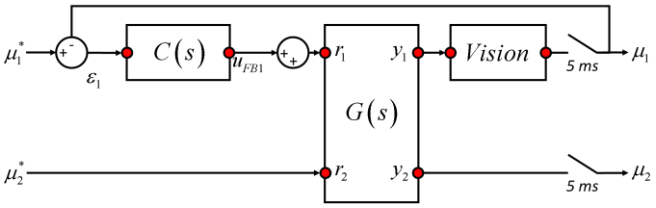

Fig. 2. A dual-state feedback control architecture. The inner loop, $G(s)$, operates at 5 kHz while the outer loop operates at 200 Hz.

The feedback controller of the outer loop, $C(s)$, assumes the form of a PI controller to ensure a zero steady state error on the position tracking. The PI gains cannot be set too high due to the limited stability margins of $G(s)$. The PI gains are heuristically tuned such that the outer loop achieves a stable tracking performance. With $K_P = 1$ and $K_I = 1$, the resulting tracking performance of the outer loop is presented in Fig. 3. Here, the web undergoes a stepping motion and simultaneously maintains a constant tension. It is assumed that each step corresponds to the period during which the fabrication process is taking place. It is therefore necessary for the web to completely settle down at the intended position before the stepping motion resumes. However, as depicted in Fig. 3, there is a slow transient response on the web position tracking. We seek to improve the position tracking performance by using Iterative Learning Control.

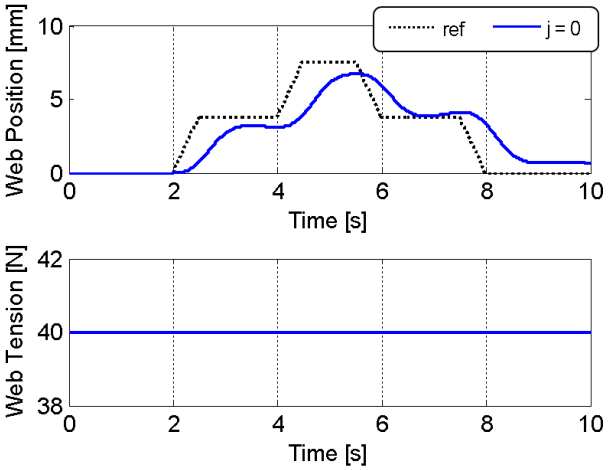

Fig 3. Tracking performance of the outer loops showing significant phase lag in the position tracking performance. The error on the tension regulation (ref = 40N) is almost negligible.

3. NOILC DESIGN AND SIMULATION

To improve the transient response of the visual servoing system of the R2R system, the outer loop architecture presented in Fig. 2 is augmented with ILC. As presented in Fig. 4, a NOILC formulation is used to update the ILC signals in the next iteration and hereafter, let j denotes the iteration index. Both the error signals ε_1^j and ε_2^j, as well as the ILC input signals at the current iteration, u_{ILC1}^j and u_{ILC2}^j are recorded in the system memory and used to update the ILC signals at the next iteration, u_{ILC1}^{j+1} and u_{ILC1}^{j+1}.

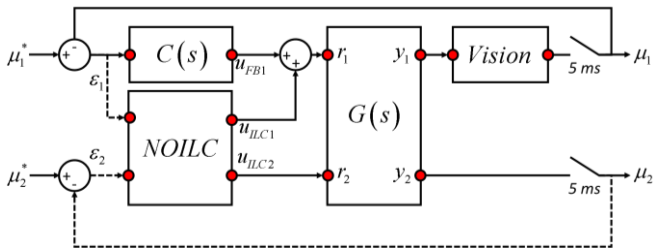

Fig. 4. A dual state feedback control architecture augmented with coupled NOILC. Error and ILC input signals from both outer loops are stored and combined to update the ILC input signals at the current iteration.

Other than error and ILC input signals from the previous iteration, the lifted NOILC formulation also requires the mapping from the ILC input signals, u_{ILC}^j to the system outputs μ^j. In the lifted form, this mapping in general is described in a form of a lower triangular Toeplitz matrix, here denoted by $\boldsymbol{P}$. The matrix $\boldsymbol{P}$ can be constructed using the finite time impulse responses of $G(s)$. In order to obtain the impulse response of the system, we must first define the transfer function from u_{ILC} to μ. According to the block diagram presented in Fig. 4, the system output μ can be defined as (2), assuming no dynamics introduced by the machine vision.

$$\begin{bmatrix} \mu_1(s) \\ \mu_2(s) \end{bmatrix} = \underbrace{\begin{bmatrix} G_{11}(s) & G_{12}(s) \\ G_{21}(s) & G_{22}(s) \end{bmatrix}}_{G(s)} \begin{bmatrix} R_1(s) \\ R_2(s) \end{bmatrix} \tag{2}$$

where

$$\begin{aligned} R_1(s) &= U_{FB1}(s) + U_{ILC1}(s) \\ R_2(s) &= U_{ILC2}(s) \end{aligned} \tag{3}$$

For convenience, the Laplace operator, s, will be dropped in the following equations. By setting μ_1^* to zero, the feedback input signals, U_{FB1}, can be written in terms of the system outputs as presented in (4).

$$U_{FB1} = -C_1\mu_1 \tag{4}$$

Substituting (3) and (4) to (2), the system outputs can be rewritten as a function of the (5).

$$\begin{aligned} \mu_1 &= G_{11}(-C_1\mu_1 + U_{ILC1}) + G_{12}U_{ILC2} \\ \mu_2 &= G_{21}(-C_1\mu_1 + U_{ILC1}) + G_{22}U_{ILC2} \end{aligned} \tag{5}$$

A slight algebraic rearrangement of (5) allows the system outputs, μ_1 and μ_2 to be explicitly expressed in terms of the ILC inputs, U_{ILC}. In (6), the matrix $\bar{G}(s)$ maps U_{ILC} to μ and the matrix entries are further described in (7).

$$\begin{bmatrix} \mu_1 \\ \mu_2 \end{bmatrix} = \underbrace{\begin{bmatrix} \bar{G}_{11} & \bar{G}_{12} \\ \bar{G}_{21} & \bar{G}_{22} \end{bmatrix}}_{\bar{G}} \begin{bmatrix} U_{ILC1} \\ U_{ILC2} \end{bmatrix} \tag{6}$$

$$\begin{aligned} \bar{G}_{11} &= \frac{G_{11}}{1+G_{11}C_1} \quad \bar{G}_{12} = \frac{G_{12}}{1+G_{11}C_1} \\ \bar{G}_{21} &= \frac{G_{21}}{1+G_{11}C_1} \quad \bar{G}_{22} = \frac{G_{22}+G_{22}G_{11}C_1 - G_{21}G_{12}C_1}{1+G_{11}C_1} \end{aligned} \tag{7}$$

Since ILC operates in the sampled data domain, $\bar{G}$ must be converted to its discrete system counterpart, $\bar{G}_D$. The conversion from the continuous to the discrete system is performed using the '*c2d*' command in Matlab with a 5 millisecond sampling time to match the sampling time of the machine vision. By invoking the *'impulse'* command on $\bar{G}_D$ in Matlab, the time series impulse responses of $\bar{G}_D$ are obtained and the corresponding plots are presented in Fig. 5. The impulse response data are essentially the system's Markov parameters, which are used to establish the input–output matrix, $\boldsymbol{P}$. The interested reader is referred to (Moore et al. 2006) for details in constructing $\boldsymbol{P}$.

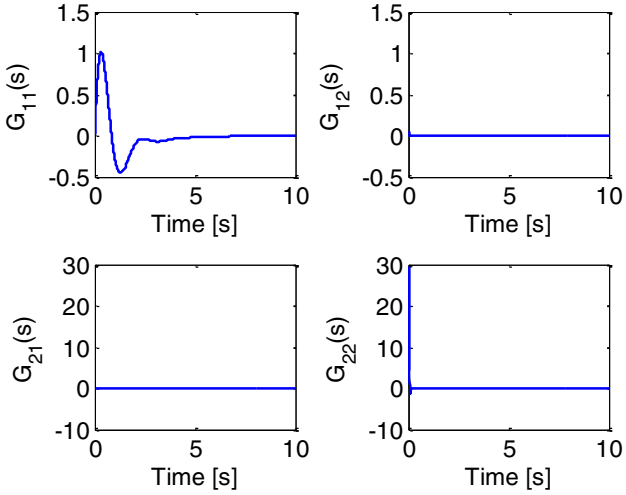

Fig. 5. The impulse responses of $\bar{G}(s)$ by which the input-output Matrix $\boldsymbol{P}$ is constructed. The web position and tension of the web are not highly coupled.

Norm Optimal ILC (NOILC) is a 2–Norm optimization framework, which minimizes a quadratic cost function described in (8), where $\boldsymbol{e}$ and $\boldsymbol{u}$ are super-vectors which defines the lifted error and ILC input signals respectively. These super-vectors are defined in (9). The resulting ILC control inputs from the quadratic optimization process, $\boldsymbol{u}^{j+1}$, are presented in (10), where L_U and L_E are the ILC learning gains, described in (11). Note that $\boldsymbol{P}^T Q \boldsymbol{P} + S + R$ must be positive definite for the solution to exist.

$$\mathcal{J} = \left\| \boldsymbol{e}^{j+1} \right\|_Q + \left\| \boldsymbol{u}^{j+1} \right\|_S + \left\| \boldsymbol{u}^{j+1} - \boldsymbol{u}^{j} \right\|_R \tag{8}$$

$$\boldsymbol{e} = \begin{bmatrix} \begin{bmatrix} \varepsilon_1(0) \\ \varepsilon_2(0) \end{bmatrix}^T & \begin{bmatrix} \varepsilon_1(1) \\ \varepsilon_2(1) \end{bmatrix}^T & \cdots & \begin{bmatrix} \varepsilon_1(N-1) \\ \varepsilon_2(N-1) \end{bmatrix}^T \end{bmatrix}^T$$

$$\boldsymbol{u} = \begin{bmatrix} \begin{bmatrix} u_{ILC1}(0) \\ u_{ILC2}(0) \end{bmatrix}^T & \begin{bmatrix} u_{ILC1}(1) \\ u_{ILC2}(1) \end{bmatrix}^T & \cdots & \begin{bmatrix} u_{ILC1}(N-1) \\ u_{ILC2}(N-1) \end{bmatrix}^T \end{bmatrix}^T \tag{9}$$

$$\boldsymbol{u}^{j+1} = L_U \boldsymbol{u}^j + L_E \boldsymbol{e}^j \tag{10}$$

$$L_U = \left(\boldsymbol{P}^T Q \boldsymbol{P} + S + R \right)^{-1} \left(\boldsymbol{P}^T Q \boldsymbol{P} + R \right)$$
$$L_E = \left(\boldsymbol{P}^T Q \boldsymbol{P} + S + R \right)^{-1} \left(\boldsymbol{P}^T Q \right) \tag{11}$$

The R2R system discussed in this article is a MIMO system with two degree of freedoms, *i.e.* the web position and tension. In designing the cost function, the emphasis on the position tracking and the tension regulation can be weighted separately by designing Q, R and S according to (12). The numerical values of $\bar{q}_i, \bar{r}_i$ and $\bar{s}_i$ used are tabulated in Table 1.

Table 1. Numerical Parameters of the NOILC Weighting

i	$\bar{q}_i$	$\bar{r}_i$	$\bar{s}_i$
1	*1000*	*10*	*1*
2	*1000*	*10*	*1*

$$Q = diag\left(\bar{Q}, \ldots, \bar{Q}\right) \in \mathbb{R}^{2N \times 2N} \quad \bar{Q} = \begin{bmatrix} \bar{q}_1 & 0 \\ 0 & \bar{q}_2 \end{bmatrix}$$
$$R = diag\left(\bar{R}, \ldots, \bar{R}\right) \in \mathbb{R}^{2N \times 2N} \quad \bar{R} = \begin{bmatrix} \bar{r}_1 & 0 \\ 0 & \bar{r}_2 \end{bmatrix} \tag{12}$$
$$S = diag\left(\bar{S}, \ldots, \bar{S}\right) \in \mathbb{R}^{2N \times 2N} \quad \bar{S} = \begin{bmatrix} \bar{s}_1 & 0 \\ 0 & \bar{s}_2 \end{bmatrix}$$

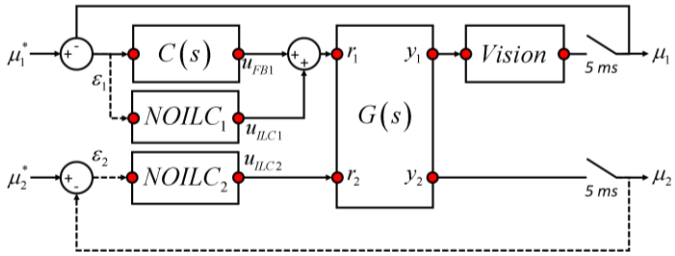

Fig. 6. A dual-layer feedback control architecture augmented with decoupled NOILC. The error and ILC input signals of the previous iteration from each outer loop are learned separately to update the ILC input signal.

Although there is some degree of coupling in $\bar{G}_D$, the magnitude of the impulse response of the off-diagonal components, as presented in the Fig. 5, are very small in comparison to the diagonal components. Assuming insignificant or zero coupling in $\bar{G}_D$, the design of u_{ILC1} and u_{ILC2} can be decoupled as illustrated in Fig. 6. The lumped input-output matrix, $\boldsymbol{P} \in \mathbb{R}^{2N \times 2N}$, can be decomposed into $\boldsymbol{P}_1 \in \mathbb{R}^{N \times N}$ and $\boldsymbol{P}_2 \in \mathrm{R}^{N \times N}$, where N denotes the trial length. The matrix $\boldsymbol{P}_1$ maps u_{ILC1} to μ_1 and by the same token $\boldsymbol{P}_2$ maps u_{ILC2} to μ_2.

In reference to (11), the NOILC learning gains L_U and L_E include the inversion of $\boldsymbol{P}^T Q \boldsymbol{P} + S + R$, which consumes a significant memory allocation. By designing u_{ILC1} and u_{ILC2} separately, a longer trial length, at least twice the size of N, may be used. The cost functions of the decoupled NOILC formulation is presented in (13), where the subscript $i \in \{1, 2\}$ corresponds to the different degree of freedoms. Here, the super-vectors of the error and ILC input signals are defined in (14) and the resulting NOILC update law is defined in (15). The weighting matrices Q_i, R_i and S_i are set as $\bar{q}_i I, \bar{r}_i I$ and $\bar{s}_i I$ respectively, where $I \in \mathbb{R}^{N \times N}$ denotes an identity matrix. The numerical values of $\bar{q}_i, \bar{r}_i$ and $\bar{s}_i$ used are exactly the same as those tabulated in Table 1.

$$\mathcal{J}_i = \left\| \boldsymbol{e}_i^{j+1} \right\|_{Q_i} + \left\| \boldsymbol{u}_i^{j+1} \right\|_{S_i} + \left\| \boldsymbol{u}_i^{j+1} - \boldsymbol{u}_i^{j} \right\|_{R_i} \tag{13}$$

$$\boldsymbol{e}_i = \begin{bmatrix} \varepsilon_i(0) & \varepsilon_i(1) & \ldots & \varepsilon_i(N-1) \end{bmatrix}^T$$
$$\boldsymbol{u}_i = \begin{bmatrix} u_{ILCi}(0) & u_{ILCi}(1) & \ldots & u_{ILCi}(N-1) \end{bmatrix}^T \tag{14}$$
$$\boldsymbol{u}_i^{j+1} = L_{U,i} \boldsymbol{u}_i^j + L_{E,i} \boldsymbol{e}_i^j$$

$$L_{U,i} = \left(\boldsymbol{P}_i^T Q_i \boldsymbol{P}_i + S_i + R_i \right)^{-1} \left(\boldsymbol{P}_i^T Q_i \boldsymbol{P}_i + R_i \right)$$
$$L_{E,i} = \left(\boldsymbol{P}_i^T Q_i \boldsymbol{P}_i + S_i + R_i \right)^{-1} \left(\boldsymbol{P}_i^T Q_i \right) \tag{15}$$

Fig. 7 contrasts the output signal of the feedback controller (FB) to the ILC output signals at the 20th iteration. Both the coupled (ILC-C) and the decoupled (ILC-D) algorithm significantly compensate for the phase lag of the feedback systems and the results of both algorithm look very similar as they overlap each other.

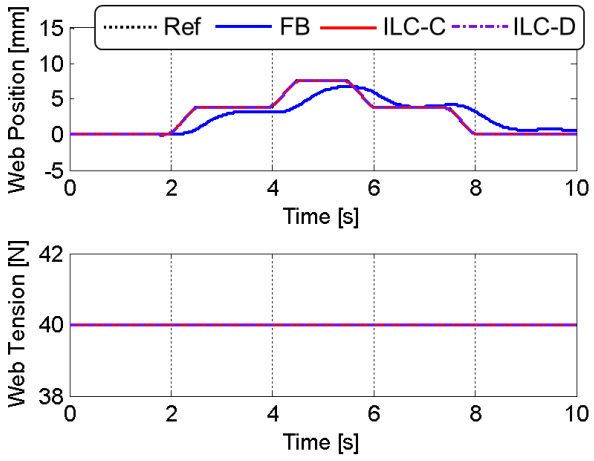

Fig. 7. Tracking performance improvement of the outer-loop. The output of the coupled and decoupled ILC look very similar at the 20th iteration

For comparison, both the normalized RMS error of the coupled ILC (RMS_i-C) and the decoupled ILC (RMS_i-D) are presented in Fig. 8. The decoupled ILC converges slightly slower in comparison to the coupled ILC because $\bar{G}_D$ is not completely decoupled. However, the RMS error on both algorithm converge to almost the same asymptotic values. The improvement on the tension regulation is almost negligible

since the R2R system already regulates the tension fairly well even when no learning is imposed. For this particular system, the simulation results suggest that the decoupled ILC provides a similar performance improvement at a lower computational cost. The performance of the decoupled system will be validated in Section 4.

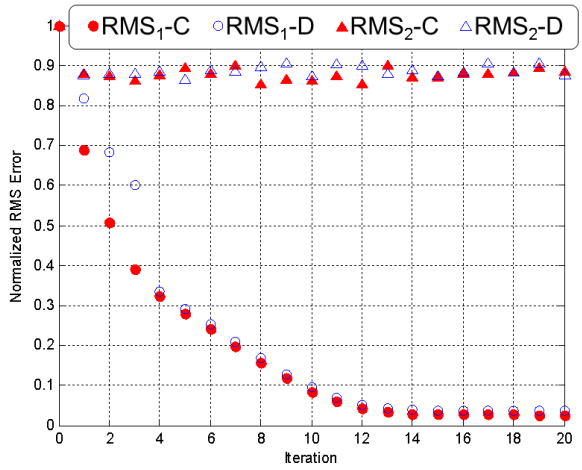

Fig. 8. Normalized RMS error plot of the outer loop. The RMS value of the error signals at each iteration are normalized against the error signals at the 0th iteration. Both the RMS Error of the coupled and decoupled NOILC converge to a very similar asymptotic value.

4. EXPERIMENTAL RESULTS

A desktop PC (Optiplex 890, Dell) is converted to a LabVIEW Real Time (RT) target and is equipped with a frame grabber (PCIe-8235, NI) and a high performance data acquisition system (PCIe-6363, NI). The images are captured using a high speed GiGE camera (Prosillica GE-680, AVT), which can acquire 200 monochrome images every second at a VGA resolution (640 pixels by 480 pixels). On the experimental setup, the image resolution is set down to 640 pixels by 50 pixels and the exposure time is set to 200 µs. With this settings, the image acquisition, image processing, and the feedback controller altogether can consistently complete the computation within 5 milliseconds. The top half of the image presented in in Fig. 9 shows the actual image acquired by the camera, while the lower half of the image is processed binary image.

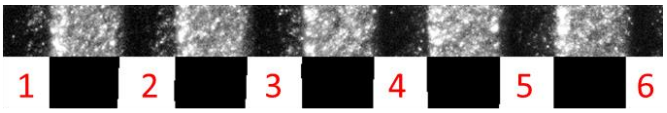

Fig. 9. The image acquired by the vision sensor. The center to center distance of the fiduciary marker is 1/64".

Several image processing steps are performed in order to obtain a usable binary image, including image thresholding, hole filling, and the removal of small particles. These image processing routines and the object analysis are programmed using the Vision Assistant software module from NI. There are 5 to 6 detected objects within the image and the object index increases starting from the leftmost detected object. Note that the object index may change as the web translates forward or backward. The relative distance of the object from the current and the previous image data, $dP(k)$, is defined in (16), where k denotes the time step index and m denotes the object index defined in (17). The position of the web, $\mu_1(k)$, according to the vision sensor is be defined in (18).

$$dP(k) = \left[\left|P_m(k) - P_3(k-1)\right|\right] \tag{16}$$

$$m = \arg\min_{m\in[2,3,4]} \left|P_m(k+1) - P_3(k)\right| \tag{17}$$

$$\mu_1(n) = \mu_1(0) + \sum_{k=0}^{n} dP(k) \tag{18}$$

Experiments are conducted to validate the performance improvement introduced by NOILC. In the experiments, the ILC input signals are generated using the decoupled NOILC algorithm. Additionally, the same reference signals used in the simulation are employed in the experiments for a more direct comparison. Fig. 10 presents the output tracking performance of the experimental system. Similar to the simulation results, the feedback controller as indicated by the blue line, produces a sluggish motion, and the tracking performance is significantly improved by the ILC signals at the 20th iteration.

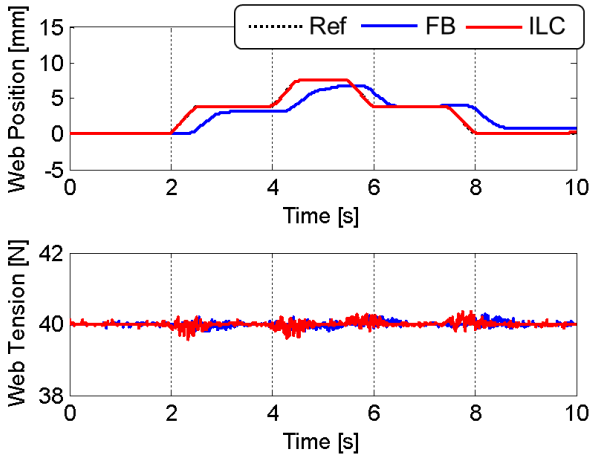

Fig. 10. The output tracking performance of the experimental system. Decoupled NOILC formulation and the vision sensor is used to improve the position tracking performance.

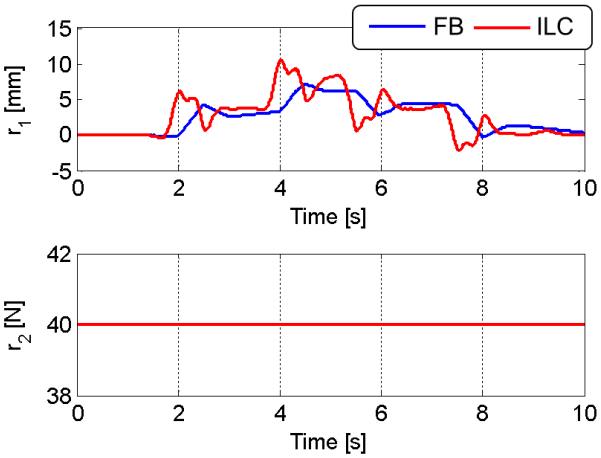

Fig. 11. ILC Input signals of the experimental system. ILC signals initiates motion earlier compared to the feedback signal.

The corresponding ILC input signals are presented in Fig 11. Here, we can observe that the non-causal nature of the NOILC generated input signals that initiates motion prior to the start and stop events in the reference signals. The normalized RMS error of the experimental system is presented in Fig. 12. At the 20th iteration, the RMS error of the web position tracking is reduced to ~5 percent of the RMS error at the 0th iteration. The experimental results validate the previous results in Section 3.

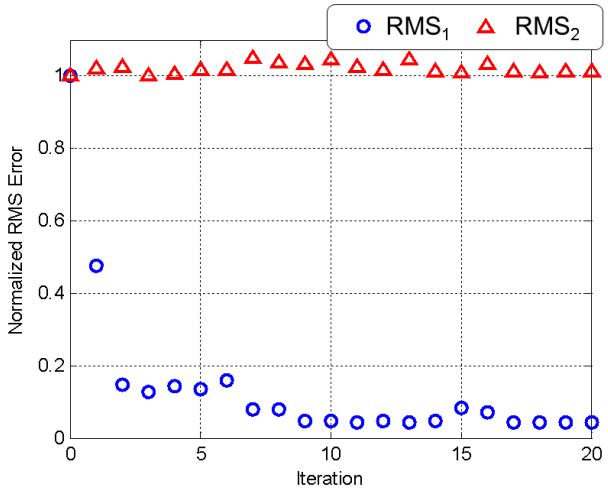

Fig. 12. Normalized RMS error plot of the outer loop. The RMS value of the error signals at each iteration are normalized against the RMS error at the 0th iteration

5. CONCLUSIONS AND FUTURE WORKS

This paper presents the coordinated position and tension control of a Roll to Roll web system using a dual state feedback architecture, where machine vision is used to visually servo the web position and tension. Norm Optimal Iterative Learning Control is augmented in the outer loops and significantly improves the position tracking of the web. Both simulation results of the coupled and the decoupled NOILC formulations for are presented in this article. Additionally, experimental results are also presented to validate the performance improvement of the proposed algorithm. It is shown that the decoupled NOILC can improve the position tracking performance of the web as well as the coupled NOILC at lower computational expense. Whilst some performance is sacrificed the tradeoff in complexity may be worthwhile.

The system in Fig. 1 is a Roll to Roll manufacturing platform that is designed to improve the scalability of the Electrohydrodynamic-Jet (E-Jet) printing process. The visual servoing approach discussed in this article is helpful to align pre-existing features on the web to the E-Jet printing's reference frame. In conjunction with the effort to improve the web handling for the R2R system, future work will demonstrate E-jet printing on the R2R system. In particular, multiple materials and systems with printed overlays will utilize the vision based servo system presented here.

ACKNOWLEDGEMENT

We acknowledge the contribution and support of the NSF Nano-CEMMS Center under award numbers CMI 07-49028.

REFERENCES

Amann, N., Owens, D. & Rogers, E., 1996. Iterative learning control for discrete-time systems with exponential rate of convergence. *IEEE Proceedings - Control Theory and Applications*, 143(2), pp.217–244.

Arimoto, S; Kawamura, S; Miyazaki, F., 1984. Bettering operation of dynamic systems by learning: A new control theory for servomechanism or mechatronics systems. In *Conference on Decision and Control*. Las Vegas: IEEE, pp. 1–6.

Barton, K. & Alleyne, A., 2008. A Cross-Coupled Iterative Learning Control Design for Precision Motion Control. *IEEE Transactions on Control Systems Technology*, 16(6), pp.1218–1231.

Barton, K. & Alleyne, A., 2010. Precision coordination and motion control of multiple systems via iterative learning control. In *American Control Conference*. Baltimore: IEEE, pp. 1272–1277.

Bristow, D.A., Tharayil, M. & Alleyne, A.G., 2006. A Survey of Iterative Learning Control. *Control Systems Magazine, IEEE*, (June), pp.96–114.

Butterworth, J.A., Pao, L.Y. & Abramovitch, D.Y., 2011. A comparison of ILC architectures for nanopositioners with applications to AFM raster tracking. In *American Control Conference*. pp. 2266–2271.

Groot Wassink, M.B. et al., 2006. Improving the drop-consistency of an inkjet printhead using meniscus-based Iterative Learning Control. In *International Conference on Control Applications*. IEEE, pp. 2830–2835.

Gunnarsson, S. & Norrlöf, M., 2001. On the design of ILC algorithms using optimization. *Automatica*, 37(2001), pp.2011–2016.

Lee, J., Lee, K. & Kim, W., 2000. Model-based iterative learning control with a quadratic criterion for time-varying linear systems. *Automatica*, 36, pp.641–657.

Moore, K., Chen, Y. & Ahn, H., 2006. Iterative learning control: A Tutorial and Big Picture View. In *IEEE Conference on Decision and Control*. San Diego: IEEE, pp. 2352 – 2357. Available at: http://ieeexplore.ieee.org/xpls/abs_all.jsp?arnumber=4178138 [Accessed October 21, 2013].

Park, J.U. & Rogers, J.A., 2012. High-Resolution Electrohydrodynamic Inkjet. In J. G. Korvink, P. J. Smith, & D. Y. Shin, eds. *Inkjet-based Micromanufacturing*. Weinheim, Germany: Wiley-VCH, pp. 57–72.

Sutanto, E. et al., 2012. A multimaterial electrohydrodynamic jet (E-jet) printing system. *Journal of Micromechanics and Microengineering*, 22(4), p.045008.

Sutanto, E. & Alleyne, A.G., 2013. Norm Optimal Iterative Learning Control for a Roll to Roll Nano/Micro-Manufacturing System. In *American Control Conference*. Washington DC: IEEE.